Images of embedded Jovian planet formation at a wide separation around AB Aurigae

Currie, T.; Lawson, K.; Schneider, G.; Lyra, W.; Wisniewski, J.; Grady, C.; ... ; Skaf, N.

Check for updates

Images of embedded Jovian planet formation at a wide separation around AB Aurigae

Thayne Currie [1,2,3] ✉, Kellen Lawson [4], Glenn Schneider [5], Wladimir Lyra[6], John Wisniewski[4], Carol Grady[3], Olivier Guyon[1,5,7], Motohide Tamura [7,8,9], Takayuki Kotani [7,8], Hajime Kawahara[10], Timothy Brandt[11], Taichi Uyama [12], Takayuki Muto[13], Ruobing Dong[14], Tomoyuki Kudo[1], Jun Hashimoto [8], Misato Fukagawa [8], Kevin Wagner [5], Julien Lozi[1], Jeffrey Chilcote[15], Taylor Tobin[15], Tyler Groff[16], Kimberly Ward-Duong[17], William Januszewski[17], Barnaby Norris [18], Peter Tuthill[18], Nienke van der Marel[19], Michael Sitko[20], Vincent Deo[1], Sebastien Vievard[1,7], Nemanja Jovanovic [21], Frantz Martinache[22] and Nour Skaf[1]

Direct images of protoplanets embedded in disks around infant stars provide the key to understanding the formation of gas giant planets such as Jupiter. Using the Subaru Telescope and the Hubble Space Telescope, we find evidence for a Jovian protoplanet around AB Aurigae orbiting at a wide projected separation (~93 au), probably responsible for multiple planet-induced features in the disk. Its emission is reproducible as reprocessed radiation from an embedded protoplanet. We also identify two structures located at 430–580 au that are candidate sites of planet formation. These data reveal planet formation in the embedded phase and a protoplanet discovery at wide, >50 au separations characteristic of most imaged exoplanets. With at least one clump-like protoplanet and multiple spiral arms, the AB Aur system may also provide the evidence for a long-considered alternative to the canonical model for Jupiter's formation, namely disk (gravitational) instability.

Almost all of the ~5,000 known indirectly detected exoplanets orbit their host stars on Solar System scales (semimajor axis <30 au)[1]. The core accretion model, in which a young gas giant forms by slowly building up a multi-Earth mass core and then by rapidly accreting protoplanetary disk gas, accounts for gas giants such as Jupiter and Saturn at these locations[2]. By contrast, directly imaged exoplanets typically have wide, 50–300 au orbits and are more than ~5 times more massive than Jupiter[3–6]. Disk conditions might not allow in situ formation for many of these planets by core accretion. A plausible alternative model is disk instability, namely a violent and rapid process of gravitational collapse that is best suited for forming supermassive gas giant planets at ~100 au (ref. [7]).

Direct images of still-forming protoplanets embedded in disks around infant stars can provide critical clues as to where and how Jovian planets on all scales form. The first incontrovertible protoplanet detections, PDS 70 bc, revealed Jovian planet formation around a near-solar-mass star[8,9] at scales (~20–35 au) smaller than the orbits of most imaged planets. Evidence of planet formation at wider separations by disk instability includes spiral density waves and spatially extended protoplanets undergoing gravitational collapse[7]. Many disks show structure potentially connected to planets

on wide separations, including spiral arms[10]. However, until now, none of these systems have shown a direct detection of protoplanets themselves. More fundamentally, the single incontrovertible protoplanetary system known so far, PDS 70 bc, probes Jovian planet formation near the final stages of assembly, where young gas giants have accreted substantial protoplanetary disk material, clearing out a cavity heavily depleted in gas and/or dust[8,9]. Detections of embedded protoplanets in gas-rich and dust-rich disks would reveal planet formation during earlier, key stages of assembly.

Results

To search for protoplanets, we conducted high-contrast imaging observations of the young, benchmark disk-bearing star AB Aurigae (AB Aur). We primarily used the Subaru Coronagraphic Extreme Adaptive Optics (SCExAO) project[11] on the Subaru Telescope between 2016 and 2020, coupled with the Coronagraphic High-Resolution Imager and Spectrograph (CHARIS) covering the major near-infrared passbands[12]. Supporting ground-based data combine SCExAO or other platforms with instruments covering complementary optical and infrared wavelengths. We also observed AB Aur with the Space Telescope Imaging Spectrograph (STIS)
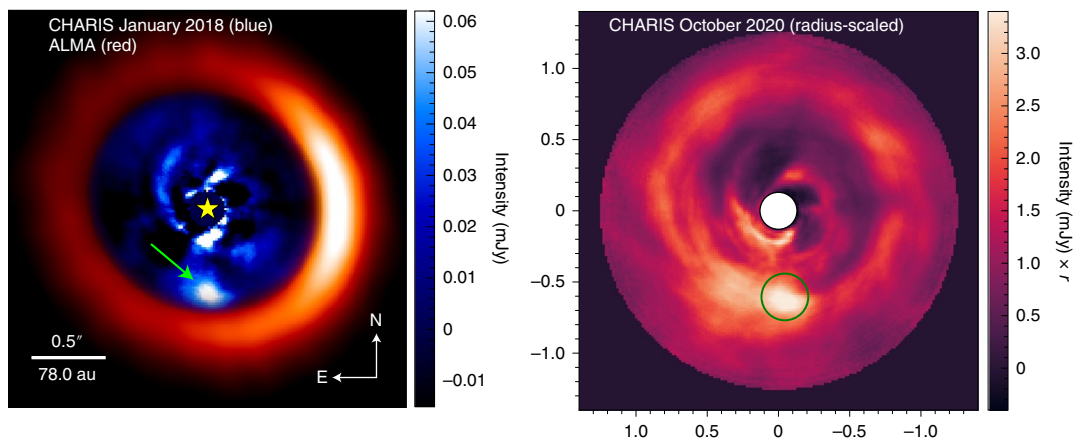
Fig. 1 | Detection of a clump-like protoplanet, AB Aur b, around AB Aur at wide separation (~93 au). Left: SCExAO/CHARIS image from 6 January 2018 combined with ALMA submillimetre imaging[13] taken in 2014 at 900 μm showing a ring of pebble-sized dust. AB Aur b lies interior to the dust ring at a location predicted from analysing spiral structure seen on smaller separations. The CHARIS component uses ADI/ALOCI for PSF subtraction. The green arrow points to the location of AB Aur b and the yellow star indicates the position of the star, AB Aur. Right: radius-scaled (that is, multiplied by *r*, the separation from the star in pixel units) CHARIS image of AB Aur from 2 October 2020 shown to highlight much fainter spiral structure in the disk. The green circle identifies AB Aur b. The CHARIS image uses polarimetry-constrained reference star subtraction to remove the stellar PSF. The colour stretch is linear in this figure and in all other figures. The *x* and *y* axes are in units of arcseconds east (along the *x* axis) and north (along the *y* axis). The white circle is the region masked by the coronagraph.

on the Hubble Space Telescope (HST) in visible light in early 2021 and reanalysed newly reprocessed archival HST data for the star from STIS (1999) and the Near Infrared Camera and Multi-Object Spectrometer (NICMOS, 2007).

Detection of AB Aur b. SCExAO/CHARIS data identify a bright concentrated emission source at an angular separation of $\rho \approx 0.59''$ (~93 au) nearly due south of the star in nine different datasets spanning four years (Table 1 and Supplementary Table 1). This source, hereafter referred to as AB Aur b, lies exterior to and is easily distinguishable from disk features detected at $\rho \approx 0.1$–$0.4''$ and spiral structure at much wider separations (Fig. 1). It is located interior to AB Aur's millimetre-resolved dust ring. Its position matches the predicted location of a protoplanet that could explain the AB Aur disk's CO gas spirals[13,14]. The CHARIS image bears a striking resemblance to gas surface density maps from simulations of Jovian planet formation on wide separations by disk instability[7,15] (Fig. 1).

Furthermore, we recover AB Aur b in archival NICMOS total intensity data in the near-infrared (1.1 μm) from 2007 and in STIS data acquired in early 2021 in visible light (0.58 μm) (Fig. 2). Visual inspection of the CHARIS, NICMOS and STIS data clearly shows that AB Aur b's position angle is changing, consistent with anticlockwise orbital motion. We easily rule out a stationary source at greater than a 5σ confidence level; a simple model of linear motion for the position of AB Aur b with time yields a reduced chi-squared close to 1.

AB Aur b's morphology, location and brightness compared to surrounding disk material cannot be due to processing artefacts. Point-spread function (PSF) subtraction using different approaches, that is, algorithms in combination with either angular differential imaging (ADI) or reference star differential imaging (RDI), recover AB Aur b with minimal evidence of photometric and astrometric biasing. Forward modelling demonstrates that subtracting a synthetic source with properties such as those we measure for AB Aur b entirely nulls the observed signal. See Methods and Supplementary Fig. 9 for more details.

Orbits. We constrained AB Aur b's orbit from its NICMOS and CHARIS astrometry using a well-tested Markov chain Monte Carlo (MCMC) code[16] (Fig. 3). This modelling suggests that the orbit

of AB Aur b is viewed ~27–58° from face-on with an eccentricity of $e \approx 0.19$–0.60 and a semimajor axis of ~45–143 au. Nearly all of these orbits do not cross the millimetre-resolved dust ring; a subset of them imply that AB Aur b is coplanar with the disk.

Morphologies. AB Aur b has a clearly defined centre, but the highest-quality data show it to be spatially resolved compared to a true point source. We estimate AB Aur b's size from multiple conservative reductions of the best datasets from CHARIS (January 2018 and October 2020) and from HST/STIS and NICMOS, which use simple reference star subtraction that is largely immune from biasing. From CHARIS data, AB Aur b has an apparent radius of $\theta \approx 0.065''$, or $\theta \approx 0.045''$ (7 au) after deconvolving with CHARIS's intrinsic PSF; this is comparable to the Hill radius of a 4 Jupiter-mass (M_J) planet at 90 au. AB Aur b has a similar intrinsic radius in the range of $\theta \approx 0.053$–$0.073''$ in the more poorly sampled STIS data.

Emission sources. AB Aur b cannot be a pure protoplanetary disk feature as its emission cannot be explained purely by scattered starlight (Fig. 4). At the same wavelengths where AB Aur b is detected in total intensity, previous and new polarized intensity imaging reveals complex disk structure but does not show concentrated emission consistent with AB Aur b[17]. The upper limit on AB Aur b's fractional polarized intensity in the near-infrared is ~20%, which is lower than the 30% of surrounding disk material[18]. Visible Aperture Masking Polarimetric Imager for Resolved Exoplanetary Structures (VAMPIRES)[19] data reveal Hα emission that may be attributed to AB Aur b. Hα emission in excess of continuum emission is usually considered to be evidence of shocked, infalling gas onto a central object or accretion onto a protoplanet. For AB Aur b, most (perhaps all) of this Hα signal may identify a scattered light component instead (Supplementary Section 5).

AB Aur b's near-infrared colours best resemble those of mid M to early L dwarfs (J–K_s = 1.14 ± 0.28)[20], which are much redder than that of a bare stellar photosphere. However, note that the scattered 'starlight' in the AB Aur disk originates not only from the 10,000 K stellar photosphere (which dominates in the optical) but also from a 1,400 K component. The latter source is caused by sub-astronomical-unit-scale gas and some dust emission and dominates in the infrared. Compared to the scaled spectrum of AB Aur
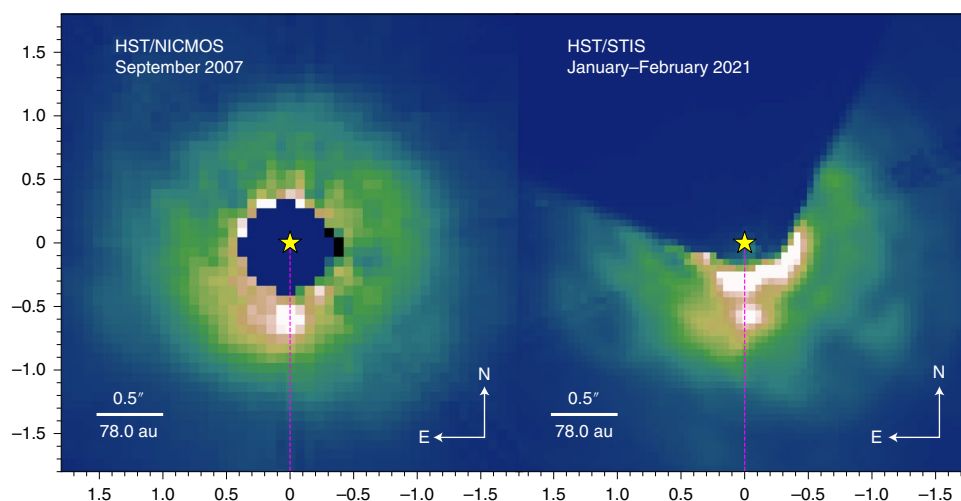
Fig. 2 | HST imaging of AB Aur over a 13-year time baseline. NICMOS F110W data from 2007 (left) and STIS/50CCD data from 2021 (right). In the NICMOS data, the coronagraph blocks the central 0.3″ region; the BAR10 occulter blocks the upper-left region of the STIS image. The dashed magenta line shows a position angle of 180°. In the 2007 (2021) data, AB Aur b lies to the left (right) of this line. The intensity scaling for both images is normalized to the peak count rate of AB Aur b: $[-29, 290]$ counts per second for NICMOS and $[-23, 230]$ counts per second for STIS. AB Aur b shows anticlockwise motion compared with the due-south position angle. The x and y axes are in units of arcseconds east (along the x axis) and north (along the y axis).
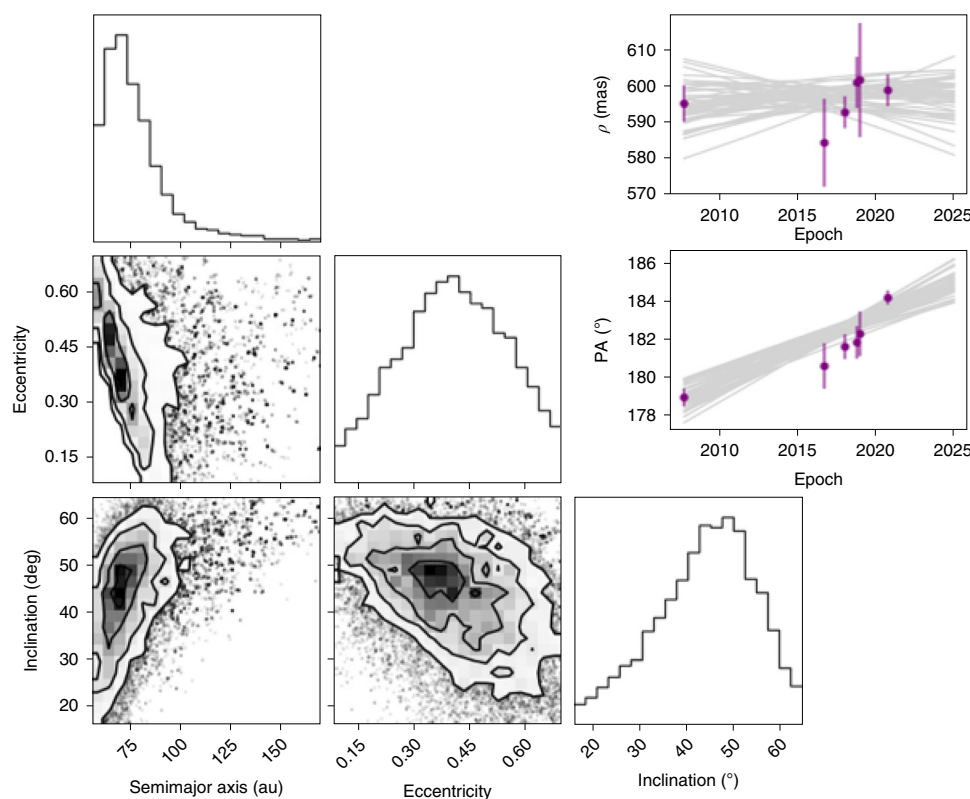
Fig. 3 | Orbit fitting results for AB Aur b. Left: corner plot showing the posterior distribution. Inset: angular separation (ρ) and position angle (PA) for the 100 best-fitting orbits as a function of epoch. The astrometric error bars are 1σ error bars.

originating from these two components ($J-K_s = 1.71 \pm 0.02$), AB Aur b is bluer in the near-infrared. It is also underluminous with STIS in visible light (where it is detected) and with the Near Infra Red Camera 2 (NIRC2) in the thermal infrared (L′; where it is not detected). AB Aur b's spectrum is consistent from epoch to epoch within errors and is bluer than that of the disk (Supplementary Figs. 10–12). AB Aur b has an apparent luminosity of $\log(L/L_\odot) \approx -2.60$

to −2.79 (where $L_\odot$ is the solar luminosity), which is comparable to that of 1-Myr-old, $10\,M_J$ planets[21,22]. Gaia and Hipparcos astrometry set a dynamical mass upper limit of ~0.13 $M_\odot$ (where $M_\odot$ is the solar mass)[23].

To reproduce AB Aur b's spectral energy distribution (SED), we considered a range of emission sources, including circumplanetary disks, bare (sub)stellar photospheres with various temperatures
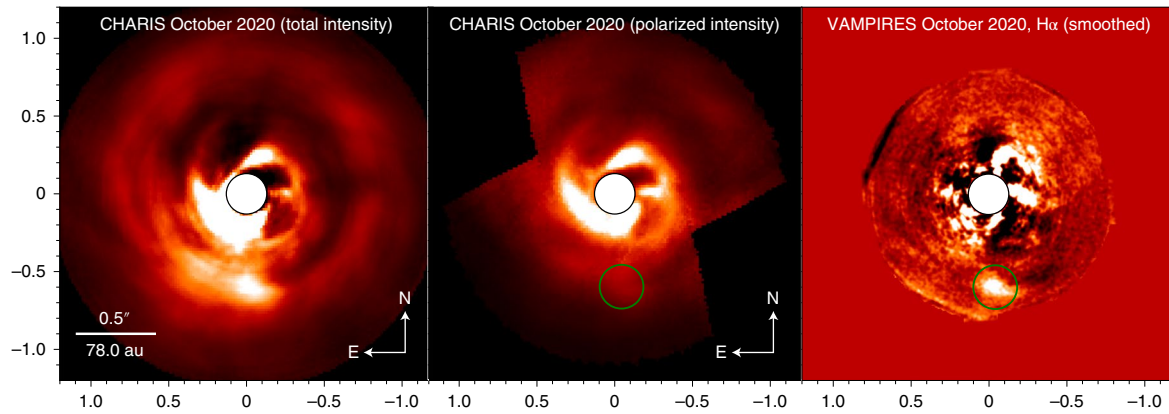
Fig. 4 | SCExAO/CHARIS images of AB Aur at different wavelengths and observing modes. Left: CHARIS total intensity wavelength-collapsed image from October 2020 (same reduction as shown in Fig. 1, right), showing a clear detection of AB Aur b. Middle: polarized intensity wavelength-collapsed image obtained one day later. A pure scattered-light disk feature would have been detected at the position of AB Aur b (green circle). Instead this region shows no concentrated emission, indicating that AB Aur b is not detected. Right: emission at the approximate position of AB Aur b from VAMPIRES Hα data using RDI/KLIP for PSF subtraction. From left to right, the intensity scaling is [0, 0.0925] mJy, [0, 0.055] mJy and [−0.007, 0.007] mJy, normalized to the source's apparent FWHM. The x and y axes are in units of arcseconds east (along the x axis) and north (along the y axis).

and gravities, and magnetospheric accretion models[24]. A dusty low-gravity atmosphere or smooth ~2,000–2,500 K blackbody combined with magnetospheric gas accretion reproduces all photometry and upper limits and matches most of the CHARIS spectrum (Supplementary Fig. 12). In the best-fit composite model that includes the planet atmosphere, the planet has a mass of $9\,M_J$, a radius of 2.75 Jupiter radii (R_J), an effective temperature of $T_{eff} = 2,200\,K$ and a surface gravity of $\log(g) = 3.5$, and is accreting at a rate of $\dot{M} \approx 1.1 \times 10^{-6}\,M_J\,yr^{-1}$. A bare photosphere does not reproduce the STIS photometry; an extended circumplanetary disk model predicts a NIRC2 detection instead of an upper limit. We emphasize that although AB Aur b's near-infrared emission is well matched by that of a planet atmosphere, a simple blackbody of comparable temperature (for example, from a circumplanetary envelope) likewise reproduces this emission. See Supplementary Sections 2 and 8 for a detailed discussion.

Detection of additional point-like features at wider separations. The HST/STIS and NICMOS data identify two additional but much fainter concentrated emission sources at wider separations of $\rho \approx 2.75''$ and $3.72''$ (429 au and 580 au). Over the nearly 22-year time interval between the STIS epochs, these sources appear in roughly the same location; they are not background objects lying behind and partially extincted by the disk. We identify no other similar sources in the STIS or NICMOS data. These sources are discussed in depth in Supplementary Section 4.

Interpretation. Despite the dissimilarity of AB Aur b's emission with scattered starlight, the SCExAO and HST images are not directly revealing only thermal emission from a planet atmosphere as is the case for the protoplanets PDS 70 b and c. AB Aur b is spatially resolved. A thermally emitting object of its size (0.045″ or ~7 au) and temperature (~2,200 K) would have a luminosity far exceeding even that of the host star. Similarly, an object with AB Aur b's luminosity and size would have a temperature of ~23 K, which is much too low to emit detectable photons in the infrared.

To explain AB Aur b's morphology and emission, we generated a synthetic image of scattered light from the AB Aur protoplanetary disk plus emission from an embedded protoplanet at the same location as AB Aur b. The protoplanet's emission is modelled as a simple blackbody of ~2,200 K with a luminosity matched to AB Aur b's observed values. The model is agnostic as to whether this emission

originates from a bare planet atmosphere or from a circumplanetary envelope or disk. AB Aur b's embedded nature may favour the latter interpretation, and emission that does not originate from a planet atmosphere is needed to explain AB Aur b's optical detections. Our simulated embedded planet appears as a slightly extended object, in agreement with our data, because protoplanetary dust located nearby scatters light from the embedded planet (Fig. 5, left). The model planet photometry (1.4 mJy) roughly matches that measured for the protoplanet at H band. The simulated image in polarized light shows no clear signal at the location of the planet, in agreement with our non-detection of AB Aur b in polarimetry (Supplementary Fig. 17).

To explain AB Aur b within the context of planet formation models, we consider a disk instability model in which a self-gravitating disk produces multiple fragments at separations comparable to those of AB Aur b. From the resulting density and temperature profiles of the disk and clump as well as from the disk scale height, we produce near-infrared scattered light images of the system. In our scattered light image, the disk-instability-formed clump produces a bright feature at the location of one clump, consistent with AB Aur b (Fig. 5, right).

Discussion

Evidence for at least one protoplanet around AB Aur at wide separations has important implications for our understanding of where planets form. Most studies analyse the demographics of imaged, fully formed planets to constrain planet formation[25,26], but the current location of an exoplanet may differ from where it formed. AB Aur b provides direct evidence that planets more massive than Jupiter can form at separations approaching 100 au, more than double the distance from the Sun to Kuiper Belt objects such as Pluto, and in striking contrast to expectations of planet formation by the canonical core accretion model.

Finally, this discovery has profound consequences for our understanding of how planets form. AB Aur b provides a key direct look at protoplanets in the embedded stage. Thus, it probes an earlier stage of planet formation than the PDS 70 system. AB Aur's protoplanetary disk shows multiple spiral arms[17,27], and AB Aur b appears as a spatially resolved clump located in proximity to these arms. These features bear an uncanny resemblance to models of Jovian planet formation by disk instability. AB Aur b may then provide direct evidence that Jovian planets can form by disk instability.
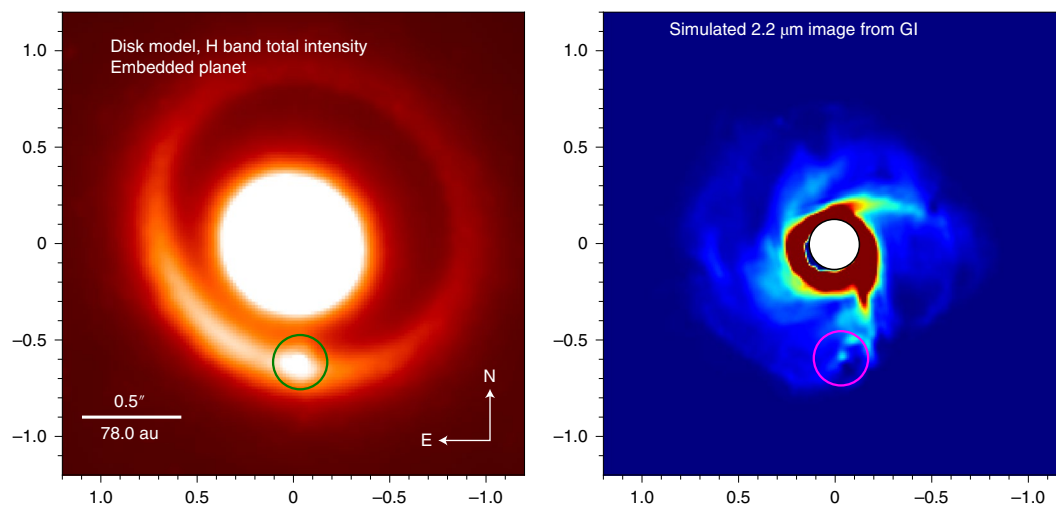
Fig. 5 | Simulating AB Aur b's emission and morphology. Left: synthetic image of AB Aur, its protoplanetary disk and an embedded AB Aur b at 1.63 µm in total intensity (−0.01 mJy to 0.041 mJy). Right: synthetic image at 2.2 µm of a self-gravitating disk forming multiple clump-like protoplanets on scales comparable to that of AB Aur b in contrast units ([0, 0.000125]). The resulting image shows a bright emission peak at the clump-like planet's location (circled). This is the densest, hottest clump in our gravitational instability (GI) simulation; other clumps created by GI are not visible because of their lower densities and/or the projection effects of the system. The x and y axes are in units of arcseconds east (along the x axis) and north (along the y axis).

An observational anchor such as the AB Aur system significantly informs the formulation of new disk instability models diagnosing the temperature, density and observability of protoplanets formed under varying conditions.

Methods

Target selection and properties. AB Aur, a $2.4 \pm 0.2\,M_\odot$ and 155.9 pc distant member of the 1–3-Myr-old Taurus–Auriga star-forming region[28–31] (Table 1), has long been considered to be a key laboratory for investigating planet formation. Optical to near-infrared scattered light imaging of its massive protoplanetary disk reveals numerous spiral arms on 200–500 au scales[32–34]. Millimetre imaging resolves a 170-au-wide ring of pebble-sized dust[15], whereas near-infrared polarimetry tracing micrometre-sized dust reveals a highly structured disk interior to this ring[17,27]; these results are consistent with dust filtration from an unseen Jovian protoplanet(s) inside the ring[35,36]. Analyses of CO gas spirals[14] suggest tidal disturbances from hitherto unseen protoplanets, including one at a position angle of ~180° and an angular separation of 0.6″.

Observations. We observed AB Aur between 2016 and 2020 with the Subaru Telescope using SCExAO, which was primarily coupled with the CHARIS integral field spectrograph in 'broadband', covering the major near-infrared passbands simultaneously (JHK, $\lambda = 1.15$–2.39 µm; spectral resolution $R \approx 20$). Except for our first (2016) epoch, we employed a Lyot coronagraph with a 0.13″ radius occulting spot to suppress scattered starlight. We obtained one set of CHARIS data in a special integral field polarimetry mode also operating in 'broadband' to better distinguish between planet and disk signals[37]. Other SCExAO data used the High-Contrast Coronographic Imager for Adaptive Optics (HiCIAO) camera in H band ($\lambda = 1.65$ µm) coupled with the vector vortex coronagraph or the VAMPIRES instrument with data split between two optical bandpasses, namely a continuum bandpass (0.64 µm) and a 1 nm-wide filter centred on Hα (0.653 µm). We also acquired thermal infrared ($\lambda = 3.78$ µm) coronagraphic imaging with the Keck II Telescope using the NIRC2 camera. All observations were conducted in ADI mode[38], allowing the sky parallactic angle and thus off-axis astrophysical objects to rotate on the detector with time to better remove the noisy stellar halo.

Total on-source integration times and parallactic angle rotations varied substantially, covering rotations of 45–136° and exposure times of 20–170 min. Weather conditions varied substantially between runs, ranging from extremely 'slow' 0.3″ optical seeing to fast, variable 1.5″ seeing. We obtained eight total intensity CHARIS datasets. Our analysis focuses on the highest-quality observations, where the observing conditions and resulting raw image quality were by far the best (18 September 2016, 6 January 2018, 16 October 2018 and 2 October 2020), although poorer-quality data do not identify any trends that undermine our conclusions.

STIS coronagraphic imaging data from 2021 cover a broad single bandpass (0.2–1.0 µm) and used the BAR10 occulter[39] with the star placed in the corner region, and consist of multiple visit-sets taken at different roll angles with interleaved observations of a colour-matched PSF reference star (HD 21062).

Archival 1999 STIS data place AB Aur behind the WedgeA1.0 position. In archival 2007 NICMOS data, the coronagraph blocks light from the AB Aur primary; the system is observed in the F110W filter and the 2.0 µm linear polarizer and coronagraph. For archival data, we followed prior publications and identified colour-matched reference PSF stars from the HST archive, namely HD 141653 for STIS and GJ 273 for NICMOS. Supplementary Section 1 clarifies some technical details unique to each observation.

Basic processing of ground-based data. From raw CHARIS images, we extracted data cubes by using the standard CHARIS cube extraction pipeline[40]. For subsequent processing we used the CHARIS data processing pipeline[41]. Additional basic processing steps, namely sky subtraction (if applicable), image registration and spectrophotometric calibration, followed previous steps. For the latter step, we used an empirical spectrum of AB Aur obtained from the SpeX spectrograph and resampled from a resolution of $R = 2,500$ to $R = 20$. AB Aur's near-infrared spectrum is far redder (J–K ≈ 1.7) than the photosphere of an A0V star (J–K ≈ 0) due to unresolved, astronomical-unit-scale hot circumstellar gas and dust[42]. Basic image processing for HiCIAO and NIRC2 data followed previous steps[43] including de-striping, bad pixel masking or correction, flat fielding, distortion correction, linearity correction and sky subtraction (for NIRC2 only), and precise image registration. For the VAMPIRES data, we dark-subtracted and then shifted each 50 ms sub-exposure to a common centre, removing 10% of the sub-exposures with the poorest adaptive-optics correction to improve the image quality of each of the co-added frames. Supplementary Section 1 describes additional technical details with our basic processing, especially with spectrophotometric calibration.

Basic processing of HST/STIS and NICMOS data. For STIS and NICMOS data, we began our reductions with the HST pipeline-produced final data products (*sx2 files for STIS and *ima files for NICMOS). After cleaning the data of cosmic rays and hot/cold pixels, we determined absolute image registration. For STIS, we used the secondary spiders. For NICMOS, acquisition images were obtained in the F187N filter, where the PSF is not undersampled. Engineering telemetry information recorded in the science frames' fits headers listed the offset from the star's position in the unoccluded acquisition images to its position behind the coronagraph (the NOFFSETXP, NOFFSETYP keywords).

PSF subtraction of ground-based data. Advanced PSF subtraction techniques can attenuate disk and protoplanet signals in highly structured disks such as AB Aur's in difficult-to-model ways, greatly exacerbating the challenge of distinguishing between these two emission sources. Therefore, we adopted the following approach.

First, for all ground-based datasets with a suitable PSF reference star, we performed reference star differential imaging (RDI) using two complementary least-squares-based methods: Karhunen–Loève image projection (KLIP) algorithm and adaptive locally optimized combination of images (ALOCI) algorithm[44–46] applied over a single region of each image (that is, 'full frame'). The nearby star HD 31233 was used as a reference PSF.

Table 1 | AB Aur system properties

Parameter	Measurement	References and remarks
AB Aur (star)		
Distance from the Sun	155.9 ± 0.04 pc; 162.9 ± 1.5 pc	Gaia EDR3 (ref. [28]), Gaia DR2 (ref. [29])
Mass	$2.4 \pm 0.2\,M_\odot$	Ref. [30]
T_{eff}	$9{,}770 \pm 100$ K	Estimated from spectral type
Luminosity	$59 \pm 5\,L_\odot$	Estimated from radiative transfer modelling
Age	1–5 Myr	Refs. [30,31]
AB Aur b		
Photometry (apparent magnitude)	$F_{cont}(0.647\,\mu m) = 1.13 \pm 0.37$ mJy $F_{H\alpha}(0.656\,\mu m) = 3.01 \pm 0.53$ mJy $m_{STIS} = 16.99 \pm 0.10$ $m_{F110W} = 15.34 \pm 0.12$ $m_J = 15.15 \pm 0.19$ $m_H = 14.56 \pm 0.18$ $m_{Ks} = 14.01 \pm 0.21$ $m_{L'} > 13.34$ (5σ)	F denotes flux density in a given passband; m denotes apparent magnitude. We adopt the average of two epochs JHK photometry from highest-quality dataset (20180106)
Epoch-averaged projected separation	$0.592'' \pm 0.010''$ (92.3 ± 1.5 au)	Average of the NICMOS, STIS and the highest-quality ground-based data
Astrometry (separation, PA, date)	$0.591'' \pm 0.011''$, $178.9° \pm 1.1°$, 20070914 $0.584'' \pm 0.012''$, $180.6° \pm 1.2°$, 20160918 $0.593'' \pm 0.004''$, $181.6° \pm 0.7°$, 20161015 $0.601'' \pm 0.007''$, $181.8° \pm 0.9°$, 20180106 $0.602'' \pm 0.016''$, $182.3° \pm 1.2°$, 20181016 $0.599'' \pm 0.005''$, $184.2° \pm 0.6°$, 20201002 $0.575'' \pm 0.020''$, $182.5° \pm 1.5°$, 20210104–20210204	NICMOS, highest-quality ground-based data and STIS
Apparent luminosity	$-2.695 \pm 0.095 \log(L/L_\odot)$	Estimated from SED modelling
Semimajor axis	93.9 au [44.6 au, 143.2 au]	Mean and 68% confidence interval from orbit fit
Eccentricity	0.40 [0.19, 0.60]	Mean and 68% confidence interval from orbit fit
Inclination	42.6° [27.1°, 58.2°]	Mean and 68% confidence interval from orbit fit
Mass estimates	$<130\,M_J$ 10–$12\,M_J$ $9\,M_J$	Estimated from dynamical mass limit Estimated from luminosity (1 Myr age) Estimated from SED modelling

Error ranges are 1σ, or taken from the literature. PA, position angle.

Second, we performed a full-frame, 'conservative' implementation of KLIP and ALOCI in combination with ADI. For CHARIS data, we set the inner and outer boundaries for PSF subtraction at $\rho \approx 0.16''$ and $1.05''$, respectively. For HiCIAO and NIRC2 data, we set the inner radius to just beyond the occulting mask edges (at $\rho \approx 0.1''$ and $0.25''$, respectively) and outer radius to $1.05''$. For VAMPIRES, we set the inner radius to $\rho \approx 0.1''$ and outer radius to $0.8''$. For all data, we imposed a rotation gap criterion of $\delta > 1$ PSF footprint to limit self-subtraction (that is, the subtraction of astrophysical signals by azimuthally displaced copies in the weighted PSF reference library). For KLIP, we retained only the first 1–5 KL modes; for ALOCI, we rewrote the covariance matrix using singular value decomposition and truncated the diagonal terms at cut-offs of 10^{-2} to 10^{-6} before inversion.

Finally, we performed 'polarimetry-constrained' RDI for one of our highest-quality datasets (CHARIS October 2020), as has been demonstrated before with CHARIS[37] and should result in near-100% throughput and no biasing of astrophysical sources. Briefly, we used the polarized intensity detection of the AB Aur disk obtained a day after this dataset to conservatively estimate total intensity using the 'diskmap' tool[47], assuming Rayleigh polarization with 100% peak fractional polarization and with disk inclination of 30° and position angle of 60° (ref. [29]). We then removed the estimate of the AB Aur total intensity disk signal for our entire observing sequence, leaving the residual signal predominantly composed of starlight from the stellar halo. Next, we performed a 'classical' RDI reduction, identifying the linear combination of the PSF reference sequence that minimized the residuals with the disk-subtracted AB Aur images. Finally, we subtracted the resulting classical reference star differential imaging (cRDI) PSF model from the original AB Aur CHARIS data (which includes the disk signal and AB Aur b) before derotating and combining the sequence as normal.

PSF subtraction of HST data. For HST data, the PSF is so stable that we can use simple, scaled reference star subtraction (namely cRDI) to suppress the stellar PSF. For both STIS and NICMOS, we used unsaturated acquisition images to determine the optimal relative flux scaling offset between AB Aur and its PSF reference star. Although the diffraction spikes are not visible in the STIS acquisition images, we verified that the registered PSF reference star position in NICMOS data minimized diffraction spider residuals in both the unsaturated and coronagraphic images. The flux rescaling in STIS matches predictions from the reference star's R and I band photometry to within 1%. For the polarimetry data, we used POLARIZE to produce Stokes Q and U images, polarized intensity images and total intensity images from each PSF subtracted image[48]. After performing PSF subtraction, we rotated each image north-up and created a master median-combined image (Supplementary Section 2).

Detection of AB Aur b. Following standard, conservative practices, we define the statistical significance of this source's detection by comparing its integrated signal within an aperture to other aperture-summed pixels at the same separation and apply a finite-element correction[43,49]. Its detections are highly statistically significant (signal-to-noise ratio (SNR) of 5–12), even when we include real astrophysical signals (that is, disk scattered light) in our noise estimate to determine the SNR. In the highest-quality ground-based data (6 January 2018 and 2 October 2020), AB Aur b has an SNR ≈ 10–12. In the poorest-quality ground-based CHARIS dataset and the poorer-sensitivity VAMPIRES data, we detect AB Aur b at SNR ≈ 5. Inspection of the reduced, sequence-combined CHARIS data cubes reveals AB Aur b in individual CHARIS spectral channels covering the J band channels through the blue half of H band (1.24–1.63 μm) for every CHARIS observation. In the highest-quality data, AB Aur b is visible in all CHARIS channels.

We recover AB Aur b in SCExAO/CHARIS, VAMPIRES and HiCIAO data using either KLIP or ALOCI algorithms in combination with either ADI or RDI (where available). We detect it in polarimetry-constrained reductions in the October 2020 data with either cRDI or RDI/KLIP. AB Aur b has a consistent morphology, location and brightness in each reduction of a given dataset. Similarly, we detect AB Aur b in the 2021 HST/STIS and 2007 NICMOS total intensity data; AB Aur b is visible in PSF subtractions in individual roll angles with a consistent morphology, location and brightness. AB Aur b is not detected in any dataset obtained in polarized light where only protoplanetary disk scattered light should be easily identifiable.

Source astrometry, photometry and spectroscopy of ground-based data. To derive precise astrometry for AB Aur b, we computed an initial centroid estimate from Gaussian fitting and then revised this estimate using a simple centre-of-light algorithm applied to background-subtracted images. The background is defined from a region surrounding source pixels, offset in radius by ~1 full-width at half-maximum (FWHM) and in azimuth by 2–3 FWHM. Supplementary Section 3 describes how we determine astrometric uncertainties.

For the CHARIS data, satellite spots of a known brightness at ~16 λ/D (where λ is wavelength and D is telescope diameter) established absolute flux calibration in each spectral channel. Instead of equating the aperture with a point-source FWHM, we adopted an eight-pixel circular aperture ($\theta \approx 0.13''$) for each channel. This aperture is comparable to the characteristic source size as measured by CHARIS; the measured encircled energy of the CHARIS PSF within 0.13″ is nearly constant (~0.6) across CHARIS's bandpass for each dataset. HiCIAO photometric calibration used neutral density filter observations of a zero-colour star (HIP 32104) instead of satellite spots but adopted the same 0.13″ aperture. The aperture used for photometry and spectral extraction was the same as that used for spectrophotometric calibration.

Forward modelling measures and corrects for signal loss in our KLIP and ALOCI reductions employed for CHARIS and HiCIAO data and helps assess upper limits for NIRC2 data. Oversubtraction (confusion of the source and speckles) is the sole source of signal loss for the reductions using RDI. For ADI reductions, signal loss can also be due to self-subtraction, namely annealing of the source in the target image by azimuthally offset copies in the reference image. For a model source intensity distribution, we adopted a simple Gaussian with an FWHM of eight pixels, which resembles the real source intensity distribution well. Forward modelling yields channel-dependent throughputs between 90% and 99% for the RDI/KLIP and ADI/ALOCI reductions used in the four highest-quality CHARIS datasets: 18 September 2016, 6 January 2018, 16 October 2018 and 2 October 2020. HiCIAO and NIRC2 data reductions have comparably high throughput.

We extracted the AB Aur photometry and spectra from CHARIS, VAMPIRES and HiCIAO data by using the same aperture adopted for spectrophotometric calibration and subtracting the same background used to constrain the source morphology. Spectra between different CHARIS epochs agree within errors. To verify our extracted source properties, we inserted a negative copy of the AB Aur b spectrum into registered, spectrophotometrically calibrated images and performed PSF subtraction with the same parameter settings used to detect the companion. AB Aur b's signal is nulled, leaving a flat background disk signal.

Astrometry and photometry of HST data. For NICMOS data, we derived an initial centroid for AB Aur b and the two wider-separation candidates by estimating using Gaussian fitting. We then generated appropriate F110W PSFs using TinyTim[50] resampled at four times the native NICMOS pixel scale. Our adopted intrinsic source temperature is 1,800 K, although differences with an A or G star template were minor, yielding an uncertainty of 5–10% in flux density. We subtracted a scaled, resampled TinyTim PSF model from the source location, varying both the brightness and position (±1 pixel for each coordinate), until the background was flattened. We then calculated the total flux for an infinite aperture based on the best-fit scaled and resampled TinyTim model. The NICMOS fits headers provided the conversion from counts per second to Jy. For the better-sampled STIS data, subtracting a simple Gaussian PSF equal to the measured source FWHM flattens the background; the fits-header-provided conversion from counts per second to Jy determined photometry for AB Aur b and wider-separation companions.

Orbit fitting. We estimated AB Aur b's orbit from astrometry obtained from NICMOS and CHARIS over a 13-year time baseline (2007 to 2020) using the sophisticated and widely used MCMC code 'orbitize!' (version 1.15.3)[16]. We adopted priors of 6.413 ± 0.1627 mas for the parallax to consider the different results from Gaia EDR3 and Gaia DR2 and adopted $2.4 \pm 0.2\,M_\odot$ for the primary mass. The Markov chains consisted of 40 temperatures for 1,000 walkers with a burn-in of 500 steps and 1,000,000 total orbits sampled. As a check on our results, we performed additional fits using MCMC with different number of orbits and walkers, or used the 'Orbits for the Impatient' (OFTI) algorithm[18] in lieu of MCMC. These fits yielded nearly identical results.

We computed the mean and 68% confidence interval from the MCMC analysis for the primary mass, parallax and orbital parameters of AB Aur b. In general, the MCMC analysis strongly favours an orbit where AB Aur b is viewed near aphelion. Although the eccentricity is relatively high (mean eccentricity of ~0.41 and 68% confidence interval of 0.25–0.56), very few of the best-fit orbits would cross the millimetre-resolved ring. The mean and 68% confidence interval for the inclination are slightly higher than the quoted literature values for the inclination of the disk, although it is possible that AB Aur b is coplanar with the outer disk, given uncertainties. Due to the small fractional sampling of AB Aur b's orbit, some other orbital parameters (for example, the longitude of the ascending node) are poorly constrained, although a subset of solutions do align with the disk position angle. Most of the orbits are consistent with the derived gas gap radius from the ^{13}CO emission, estimated to be between 64 au and 98 au (ref. [13]). The ^{13}CO gap is well inside the dust cavity, just as seen in other transition disks, consistent with a gap cleared by a companion with the dust trapped at the outer edge of the gap[51].

Spectroscopic analysis. To assess whether AB Aur b is compatible with pure protoplanetary disk scattered light, we compared its optical to mid-infrared SED to a scaled stellar spectrum. The optical portion of the spectrum is an A0V model reddened by Av = 0.5 and matched to AB Aur's broadband photometry; the near- to mid-infrared portion draws from the SpeX spectrum. The AB Aur b spectrum shows substantial differences with the model scaled stellar spectrum over all wavelengths. Its optical emission from STIS is underluminous compared to scattered starlight; its mid-infrared upper limit from NIRC2 is a factor of three fainter than the predicted brightness for scattered light. The slope of the CHARIS spectrum is also bluer than scattered light (Supplementary Figs. 12 and 13).

Modelling the emission of AB Aur b. To compare AB Aur b to observational predictions for a simple embedded planet model, we generated spectra for combinations of several different emission sources: circumplanetary disk models spanning a range of planet masses (1–15 M_J), accretion rates (10^{-5}–$10^{-8}\,M_J\,yr^{-1}$), disk inner radii (1–10 R_J) and magnetic field strengths (10–100 G)[21,24]. Instead of a planet atmosphere, we separately considered simple blackbody emission with temperatures comparable to that expected for young planets (~1,000–3,000 K)[21].

To provide an explanation for the appearance of AB Aur b as an extended, embedded object, we used the Monte Carlo radiative transfer code MCMax3D to produce synthetic images of protoplanetary disk scattered light, thermal emission from AB Aur b[52], and light scattered by the disk from AB Aur b in the near-infrared (where AB Aur b and the highly structured disk are detected) and the millimetre (where only a small dust component near the star plus a ring of cold dust is detected). The embedded planet model adopts a source luminosity of $\log(L/L_\odot) \approx -2.60$ and temperature of 2,200 K embedded in AB Aur's protoplanetary disk. We adjust properties of the protoplanetary disk (for example, scale height or dust mass) to match its characteristic near-infrared scattered light brightness near the location of AB Aur b. To simultaneously match the millimetre ring imaged by the Atacama Large Millimeter/submillimeter Array (ALMA), we added a second disk component lying just exterior to AB Aur b. We convolved the model near-infrared image with the CHARIS PSF. Because of the protoplanetary disk's low optical depth in our model ($\tau \approx 1.3$ in H band), the model planet's signal is simply spread out over a large area, not significantly attenuated. The planet's intrinsic light may be further extincted by dust in a circumplanetary disk.

To link the appearance of the AB Aur system as a whole to models for planet formation, we generated a simple, proof-of-concept hydrodynamical disk instability model. The model consists of a self-gravitating two-dimensional global disk, ranging from 30 au to 300 au, with a gravitational unstable range between 50 au and 150 au. To simulate planet formation by disk instability we used the PENCIL code[53]. The resolution is 432 × 864 in radius and azimuth, respectively. A few orbits into the simulation, the disk fragments into several (~10) clumps of the order of the mass of Jupiter, consistent with the Bonnor–Ebert mass of the system at 100 au (~0.97 M_J). To produce a synthetic image, we performed full radiative transfer post-processing with RADMC-3D[54]; we included the stellar blackbody, and chose one of the embedded clumps to also be a source of photons, with a radius of two Jupiter radii and a central temperature of 5,000 K. Scattering was treated as isotropic. As the photons travel from the source to the atmosphere, they are successively scattered, absorbed, reemitted and thermalized at a lower effective temperature.

Data availability

With the exception of data from the first CHARIS epoch (obtained during engineering observations), all raw SCExAO data are available for public download from the Subaru SMOKA archive: https://smoka.nao.ac.jp/. The first epoch data are available upon request. Keck data are available from the Keck Observatory Archive (https://koa.ipac.caltech.edu/cgi-bin/KOA/nph-KOAlogin); HST data are available from the Milkulski Archive for Space Telescopes (https://archive.stsci.edu/missions-and-data/hst). Processed data are made available from the corresponding author upon reasonable request.

Code availability

Data reduction pipelines used to create CHARIS data cubes and perform subsequent processing are publicly available on GitHub (https://github.com/PrincetonUniversity/charis-dep and https://github.com/thaynecurrie/charis-dpp).

References

1. Borucki, W. et al. Kepler planet-detection mission: introduction and first results. *Science* **327**, 977–980 (2010).
2. Pollack, J. B. et al. Formation of the giant planets by concurrent accretion of solids and gas. *Icarus* **124**, 62–85 (1996).
3. Marois, C. et al. Direct imaging of multiple planets orbiting the star HR 8799. *Science* **322**, 1348–1352 (2008).
4. Carson, J. Direct imaging discovery of a 'super-Jupiter' around the late B-type star κ And. *Astrophys. J. Lett.* **763**, L32 (2013).
5. Currie, T. et al. Direct imaging and spectroscopy of a candidate companion below/near the deuterium-burning limit in the young binary star system, ROXs 42B. *Astrophys. J. Lett.* **780**, L30 (2014).
6. Chauvin, G. et al. Discovery of a warm, dusty giant planet around HIP 65426. *Astron. Astrophys.* **605**, L9 (2017).
7. Boss, A. P. Evolution of the solar nebula. IV. Giant gaseous protoplanet formation. *Astrophys. J.* **503**, 923–937 (1998).
8. Keppler, M. et al. Discovery of a planetary-mass companion within the gap of the transition disk around PDS 70. *Astron. Astrophys.* **617**, A44 (2018).
9. Haffert, S. Y. et al. Two accreting protoplanets around the young star PDS 70. *Nat. Astron.* **3**, 749–754 (2019).
10. Muto, T. et al. Discovery of small-scale spiral structures in the disk of SAO 206462 (HD 135344B): implications for the physical state of the disk from spiral density wave theory. *Astrophys. J. Lett.* **748**, L22 (2012).
11. Jovanovic, N. et al. The Subaru Coronagraphic Extreme Adaptive Optics System: enabling high-contrast imaging on solar-system scales. *Publ. Astron. Soc. Pac.* **127**, 890 (2015).
12. Groff, T. D. et al. Laboratory testing and performance verification of the CHARIS integral field spectrograph. *Proc. SPIE* **9908**, 99080O (2016).
13. van der Marel, N. et al. On the diversity of asymmetries in gapped protoplanetary disks. *Astron. J.* **161**, 33 (2021).
14. Tang, Y.-W. et al. Planet formation in AB Aurigae: imaging of the inner gaseous spirals observed inside the dust cavity. *Astrophys. J.* **840**, 32 (2017).
15. Vorobyov, E., Zakhozhay, O. & Dunham, M. Fragmenting protostellar discs: properties and observational signatures. *Mon. Not. R. Astron. Soc.* **433**, 3256–3273 (2013).
16. Blunt, S. et al. orbitize!: a comprehensive orbit-fitting software package for the high-contrast imaging community. *Astron. J.* **159**, 89 (2020).
17. Hashimoto, J. et al. Direct imaging of fine structures in giant planet-forming regions of the protoplanetary disk around AB Aurigae. *Astrophys. J. Lett.* **729**, L17 (2011).
18. Perrin, M. D. et al. The case of AB Aurigae's disk in polarized light: is there truly a gap? *Astrophys. J. Lett.* **707**, L132–L136 (2009).
19. Norris, B. et al. The VAMPIRES instrument: imaging the innermost regions of protoplanetary discs with polarimetric interferometry. *Mon. Not. R. Astron. Soc.* **447**, 2894–2906 (2015).
20. Pecaut, M. J. & Mamajek, E. E. Intrinsic colors, temperatures, and bolometric corrections of pre-main-sequence stars. *Astrophys. J. Suppl. Ser.* **208**, 9 (2013).
21. Spiegel, D. S. & Burrows, A. Spectral and photometric diagnostics of giant planet formation scenarios. *Astrophys. J.* **745**, 174 (2012).
22. Baraffe, I., Chabrier, G., Barman, T. S., Allard, F. & Hauschildt, P. Evolutionary models for cool brown dwarfs and extrasolar giant planets. The case of HD 209458. *Astron. Astrophys.* **402**, 701–712 (2003).
23. Brandt, T. D. The Hipparcos–Gaia Catalog of Accelerations: Gaia EDR3 edition. *Astrophys. J. Suppl. Ser.* **254**, 42 (2021).
24. Zhu, Z. Accreting circumplanetary disks: observational signatures. *Astrophys. J.* **799**, 16 (2015).
25. Wagner, K., Apai, D. & Kratter, K. M. On the mass function, multiplicity, and origins of wide-orbit giant planets. *Astrophys. J.* **877**, 46 (2019).
26. Forgan, D. & Rice, K. Towards a population synthesis model of objects formed by self-gravitating disc fragmentation and tidal downsizing. *Mon. Not. R. Astron. Soc.* **432**, 3168–3185 (2013).
27. Boccaletti, A. et al. Possible evidence of ongoing planet formation in AB Aurigae. A showcase of the SPHERE/ALMA synergy. *Astron. Astrophys.* **637**, L5 (2020).
28. Gaia Collaboration Gaia Early Data Release 3. Summary of the contents and survey properties. *Astron. Astrophys.* **649**, A1 (2021).
29. Gaia Collaboration Gaia Data Release 2. Summary of the contents and survey properties. *Astron. Astrophys.* **616**, A1 (2018).
30. deWarf, L. E., Sepinsky, J. F., Guinan, E. F., Ribas, I. & Nadalin, I. Intrinsic properties of the young stellar object SU Aurigae. *Astrophys. J.* **590**, 357–367 (2003).
31. Kenyon, S. J., Gomez, M. & Whitney, B. A. in *Handbook of Star Forming Regions: Volume I, The Northern Sky* (ed. Reipurth, B) 405–458 (Astronomical Society of the Pacific, 2008).
32. Grady, C. et al. Hubble Space Telescope Space Telescope Imaging Spectrograph coronagraphic imaging of the Herbig AE star AB Aurigae. *Astrophys. J. Lett.* **523**, L151–L154 (1999).
33. Oppenheimer, B. R. et al. The Solar System-scale disk around AB Aurigae. *Astrophys. J.* **679**, 1574–1581 (2008).
34. Fukagawa, M. et al. Spiral structure in the circumstellar disk around AB Aurigae. *Astrophys. J. Lett.* **605**, L53–L56 (2004).
35. Dong, R. The missing cavities in the SEEDS polarized scattered light images of transitional protoplanetary disks: a generic disk model. *Astrophys. J.* **750**, 161 (2012).
36. Zhu, Z., Nelson, R. P., Dong, R., Espaillat, C. & Hartmann, L. Dust filtration by planet-induced gap edges: implications for transitional disks. *Astrophys. J.* **755**, 6 (2012).
37. Lawson, K. et al. High-contrast integral field polarimetry of planet-forming disks with SCExAO/CHARIS. *Proc. SPIE* **11823**, 118230D (2021).
38. Marois, C., Lafrenière, D., Doyon, R., Macintosh, B. & Nadeau, D. Angular differential imaging: a powerful high-contrast imaging technique. *Astrophys. J.* **641**, 556–564 (2006).
39. Debes, J. H., Ren, B. & Schneider, G. Pushing the limits of the coronagraph occulters on Hubble Space Telescope/Space Telescope Imaging Spectrograph. *J. Astron. Telesc. Instrum. Syst.* **5**, 035003 (2019).
40. Brandt, T. D. et al. Data reduction pipeline for the CHARIS integral-field spectrograph I: detector readout calibration and data cube extraction. *J. Astron. Telesc. Instrum. Syst.* **3**, 048002 (2017).
41. Currie, T. et al. No clear, direct evidence for multiple protoplanets orbiting LkCa 15: LkCa 15 bcd are likely inner disk signals. *Astrophys. J. Lett.* **877**, L3 (2019).
42. Tannirkulam, A. A tale of two Herbig Ae stars, MWC 275 and AB Aurigae: comprehensive models for spectral energy distribution and interferometry. *Astrophys. J.* **689**, 513–531 (2008).
43. Currie, T. et al. A combined Subaru/VLT/MMT study of planets orbiting HR 8799: implications for atmospheric properties, masses, and formation. *Astrophys. J.* **729**, 128 (2011).
44. Soummer, R., Pueyo, L. & Larkin, J. Detection and characterization of exoplanets and disks using projections on Karhunen–Loève eigenimages. *Astrophys. J. Lett.* **755**, L28 (2012).
45. Currie, T. et al. Direct imaging confirmation and characterization of a dust-enshrouded candidate exoplanet orbiting Fomalhaut. *Astrophys. J. Lett.* **760**, L32 (2012).
46. Currie, T. et al. Resolving the HD 100546 protoplanetary system with the Gemini Planet Imager: evidence for multiple forming, accreting planets. *Astrophys. J. Lett.* **814**, L27 (2015).
47. Stolker, T. et al. Scattered light mapping of protoplanetary disks. *Astron. Astrophys.* **596**, A70 (2016).
48. Hines, D. C., Schmidt, G. D. & Schneider, G. Analysis of polarized light with NICMOS. *Publ. Astron. Soc. Pac.* **112**, 983–995 (2000).
49. Mawet, D. Fundamental limitations of high contrast imaging set by small sample statistics. *Astrophys. J.* **792**, 97 (2014).
50. Krist, J. in *Astronomical Data Analysis Software and Systems IV* (eds Shaw, R. A. et al.) 349–352 (Astronomical Society of the Pacific, 1995)
51. Pinilla, P. et al. Trapping dust particles in the outer regions of protoplanetary disks. *Astron. Astrophys.* **538**, A114 (2012).
52. Min, M., Dullemond, C. P., Dominik, C., de Koter, A. & Hovenier, J. W. Radiative transfer in very optically thick circumstellar disks. *Astron. Astrophys.* **497**, 155–166 (2009).
53. Brandenburg, A. & Dobler, W. Hydromagnetic turbulence in computer simulations. *Comput. Phys. Commun.* **147**, 471–475 (2002).
54. Dullemond, C., Juhasz, A. & Pohl, A. RADMC-3D: a multi-purpose radiative transfer tool. *Astrophysics Source Code Library* ascl:1202.015 (2012).

Author contributions

T.C. conceived of the project, (co-)led the total intensity data reduction, performed the spectroscopic and orbital analysis, and wrote the manuscript. K.L. and J.W. led the polarized intensity data reduction and the polarimetry-constrained PSF subtraction method for CHARIS. G.S. planned the STIS observations and co-led the HST/STIS and NICMOS reductions. W.L. generated the hydrodynamical models used to compare the real data with models of planet formation. C.G. aided with project and observing planning. O.G., J.L., S.V., V.D., N.J., F.M. and N.S. oversaw the operation of SCExAO. M.T. provided project management. T.K and H.K. planned and obtained one epoch of CHARIS data. T.B. provided dynamical mass estimates. T.U. and B.N. contributed VAMPIRES data reduction steps. R.D. and T.M. aided with interpreting planet-induced disk features. J.C., T.T. and T.G. lead the operation and maintenance of CHARIS. K.W.-D. and W.J. planned the STIS observations. N.v.d.M. provided the AB Aur ALMA image. M.S. obtained SpeX data. The authors all contributed to the original observing proposals, data acquisition and/or paper draft comments.

Competing interests

The authors declare no competing interests.

Additional information

Supplementary information The online version contains supplementary material available at https://doi.org/10.1038/s41550-022-01634-x.

Correspondence and requests for materials should be addressed to Thayne Currie.

Peer review information *Nature Astronomy* thanks the anonymous reviewers for their contribution to the peer review of this work

Reprints and permissions information is available at www.nature.com/reprints.

Publisher's note Springer Nature remains neutral with regard to jurisdictional claims in published maps and institutional affiliations.

© The Author(s), under exclusive licence to Springer Nature Limited 2022